JACS
JOURNAL OF THE AMERICAN CHEMICAL SOCIETY
Article
pubs.acs.org/JACS

Recycling Nicotinamide. The Transition-State Structure of Human Nicotinamide Phosphoribosyltransferase

Emmanuel S. Burgos, Mathew J. Vetticatt, and Vern L. Schramm*

Department of Biochemistry, Albert Einstein College of Medicine, 1300 Morris Park Avenue, Bronx, New York 10461, United States

Supporting Information

ABSTRACT: Human nicotinamide phosphoribosyltransferase (NAMPT) replenishes the NAD pool and controls the activities of sirtuins, mono- and poly-(ADP-ribose) polymerases, and NAD nucleosidase. The nature of the enzymatic transition-state (TS) is central to understanding the function of NAMPT. We determined the TS structure for pyrophosphorolysis of nicotinamide mononucleotide (NMN) from kinetic isotope effects (KIEs). With the natural substrates, NMN and pyrophosphate (PPi), the intrinsic KIEs of [1′-^{14}C], [1-^{15}N], [1′-^{3}H], and [2′-^{3}H] are 1.047, 1.029, 1.154, and 1.093, respectively. A unique quantum computational approach was used for TS analysis that included structural elements of the catalytic site. Without constraints (e.g., imposed torsion angles), the theoretical and experimental data are in good agreement. The quantum-mechanical calculations incorporated a crucial catalytic site residue (D313), two magnesium atoms, and coordinated water molecules. The TS model predicts primary ^{14}C, α-secondary ^{3}H, β-secondary ^{3}H, and primary ^{15}N KIEs close to the experimental values. The analysis reveals significant ribocation character at the TS. The attacking PPi nucleophile is weakly interacting (r_{C-O} = 2.60 Å), and the *N*-ribosidic C1′−N bond is highly elongated at the TS (r_{C-N} = 2.35 Å), consistent with an A_ND_N mechanism. Together with the crystal structure of the NMN·PPi·Mg_2·enzyme complex, the reaction coordinate is defined. The enzyme holds the nucleophile and leaving group in relatively fixed positions to create a reaction coordinate with C1′-anomeric migration from NAM to the PPi. The TS is reached by a 0.85 Å migration of C1′.

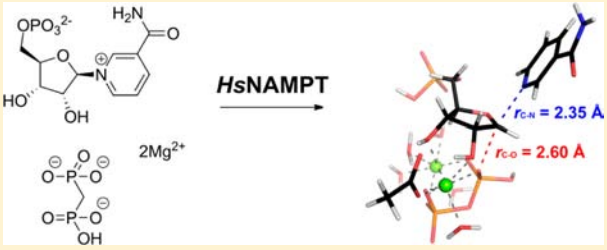

INTRODUCTION

NAD is an important coenzyme for redox reactions as well as the substrate for regulatory NAD-linked enzymes. The poly-(ADP-ribose) polymerases (PARP) (Figure 1a) are responsible for post-translational modifications of proteins by transfer of ADP-ribose (ADPR) to an amino acid acceptor of the target.[1] Involved in DNA damage detection and repair, their role is decisive for the maintenance of the genomic stability.[2] The second family includes the silent information regulator 2 (Sir2), initially characterized in yeast.[3] Homologues of Sir2, SIRT1, and six other sirtuins (SIRT) encoded in the human genome, catalyze the NAD-dependent deacetylation of histones and transcription factors (e.g., p53, FOXO; Figure 1a).[4] Enhanced SIRT1 activity, along with high concentrations of NAD, have been correlated with resistance to oxidative stress.[5] Deacetylations of FOXO[6] and p53[7] promote lifespan extension through inhibition of apoptosis, reduction of damages from oxidative stress and mediating the up-regulation of manganese superoxide dismutase (MnSOD), catalase,[8] and thioredoxin[9] (Figure 1a). NAD nucleosidase (CD38) catalyzes the hydrolysis of NAD to ADPR and nicotinamide (NAM) and is also responsible for the production of cyclic ADPR (*c*ADPR),[10] a signaling molecule with Ca^{2+}-mobilizing activity (Figure 1a).

Cellular NAD consumption is high, and constant recycling is required to sustain the activities of these enzymes. In mammals, nicotinate mononucleotide (NAMN) and nicotinamide mononucleotide (NMN) are precursors of NAD (Figure 1a). Although NAD can arise from nicotinate (NA) salvage or *de novo* synthesis from L-tryptophan (Figure 1a), its biosynthesis is predominantly achieved by nicotinamide phosphoribosyltransferase (NAMPT) in recycling NAM from SIRT, PARP and CD38 reactions (Figure 1). NAMPT catalyzes the rate limiting step in NAD salvage, a documented role in human metabolism.[11] It is linked to the function of sirtuins through modulation of NAD synthesis.[12] NAMPT inhibition causes reduced levels of NAD and induces premature senescence, while its overexpression inhibits cell death.[13] NAMPT is up-regulated in several cancers where NF-κB, IL-6, and nitric oxide synthase promote angiogenesis (Figure 1a).[14−17]

NAMPT has been validated as a cancer target by the inhibitor FK866 (Figure 2).[18] Crystallographic studies[19,20] and mechanistic insights[21] on NAMPT-catalyzed NMN synthesis provide a functional description of this target and have promoted the search for more powerful inhibitors. Despite the description of additional drugs (e.g., GMX1778, Figure 2), the *in vivo* inhibition of this enzyme is difficult because (a) modest NAMPT inhibitors are ineffective at physiological concentrations of NAM[18,22] and (b) enzyme mutations occur

Received: October 15, 2012
Published: February 2, 2013

   dx.doi.org/10.1021/ja310180c | J. Am. Chem. Soc. 2013, 135, 3485−3493

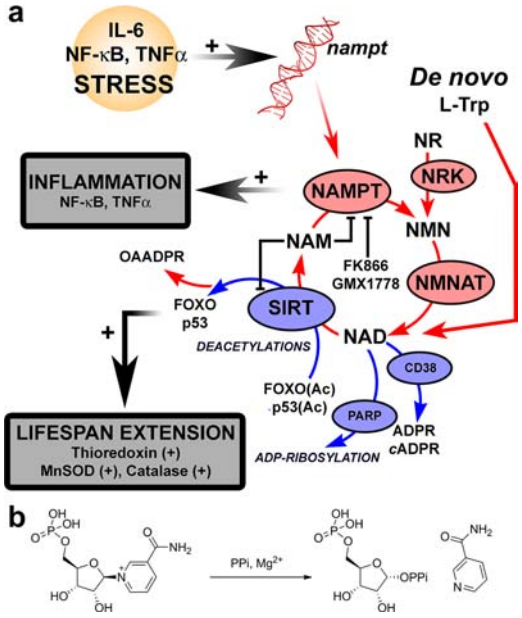

Figure 1. Role of NAMPT in mammalian NAD metabolism. (a) Salvage of NAD (red labels) is predominantly performed by NAMPT, the rate-limiting formation of NMN from NAM and PRPP. NMN is converted to NAD by three isoforms of NMN adenylyltransferase (NMNAT, EC 2.7.7.1). NMN can also arise from phosphorylation of nicotinamide riboside (NR), an additional salvageable NAD precursor (nicotinamide riboside kinase; NRK, EC 2.7.1.22). Other ways to generate NAD include its salvage from NA and the *de novo* synthesis from L-Trp. The NAD pool needs constant replenishment because of NAD use (blue labels). Lifespan extension may be promoted by SIRT1 through FOXO/p53 deacetylation. Stress stimuli (IL-1β) enhances NAD production through NAMPT overexpression. Likewise, STAT 3 (through an IL-6 signaling pathway), NF-κB, and TNFα up-regulate *nampt* (red DNA). PGE2 is implicated in arthritis (via mPGES-1 up-regulation). FK866 and GMX17778 inhibit NAMPT. (b) Pyrophosphorolysis reaction catalyzed by NAMPT.

and result in a 20 000-fold loss of efficiency for this class of compounds.[23]

Kinetic isotope effects (KIEs) provide the only experimental approach to deliver atomic-level information of the transition-state (TS) structure (bond distances, angles, and charges). Here we measured the intrinsic KIEs for the pyrophosphorolysis reaction catalyzed by human NAMPT (Figure 1b) and used a complementary quantum chemical approach to establish the TS structure from the experimental data. The TS structure and its electrostatic potential surface (ESPS) provide an unprecedented tool for understanding catalysis and to provide a blueprint for the design of TS analogues.

MATERIALS AND METHODS

Protein Expression and Purification. Human NAMPT was expressed and purified as previously described.[21] A pBAD vector encoding for the ribokinase from *E. coli* was kindly provided by Dr. Sherry L. Mowbray (Swedish University of Agricultural Sciences, Uppsala, Sweden); the protein expression and purification were performed as reported.[24] A pTEV6 plasmid encoding for *Salmonella enterica* PncA nicotinamidase (with a *N*-terminal maltose-binding protein-hexahistidine tag) was the generous gift of Dr. Jorge C. Escalante-Semerena (University of Wisconsin, Madison); the protein was expressed and purified as previously described.[25]

Isotopic Labeling of NMN Substrates and Purification. [5′-^{3}H]NMN, [5′-^{14}C]NMN, [4′-^{3}H]NMN, [1′-^{14}C]NMN, and [1′-^{3}H]NMN were synthesized enzymatically from [6-^{3}H]glucose,

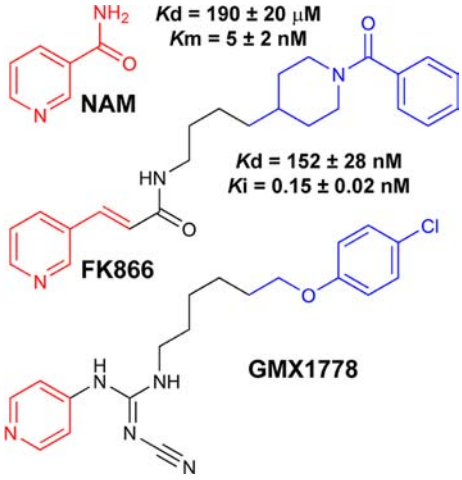

Figure 2. Similarities between NAM and NAMPT inhibitors. In the NAMPT active site, NAM interacts with Tyr*18 and Phe193 in a π-stacking fashion (PDB: 3DKJ).[19] FK866 resembles NAM; its pyridyl group (red) also interacts with NAMPT at the Tyr*18 and Phe193 levels. Additional interactions inside a β-barrel (β7, β8, β11, and β12) are provided by the peptidic moiety (black) while hydrophobic interactions are ensured by the "tail" of the inhibitor (blue). No structure for NAMPT-bound GMX1778 has been reported, but its relation to FK866 suggests similar interactions. Parameters such as K_m, K_d, and K_i are given for a better illustration of these similarities.[11,20]

[6-^{14}C]glucose, [5-^{3}H]glucose, [1-^{14}C]ribose, and [1-^{3}H]ribose, respectively (purchased from American Radiolabeled Chemicals Inc. and Moravek Biochemicals), as shown in Figure S1a. A detailed protocol is available in the Supporting Information. [2′-^{3}H]NMN and [1-^{15}N,5′-^{14}C]NMN were synthesized from [2-^{3}H]ribose (Figure S1b) and [1-^{15}N]NAM (Figure S1c), whose syntheses are described in the Supporting Information.

Kinetic Isotope Effect Measurements—Experimental KIEs. KIEs were measured under competitive conditions using the isotope ratio method.[26] The isotopic label of interest was mixed with the appropriate remote label (the [5′-^{14}C]NMN being the remote label used for all ^{3}H KIEs while the [5′-^{3}H] and [4′-^{3}H]NMN were used as the remote labels for all other KIEs). The ^{3}H to ^{14}C cpm ratio was 1:1, with no less than 4×10^5 cpm of ^{14}C per experiment. The reaction mixture (2 mL) contained 50 mM MES (pH 6.30), 100 mM KCl, 5 mM $MgCl_2$, 1 mM tris(hydroxypropyl)phosphine (THP), 75 μM pyrophosphate (PPi), and 25 μM NMN (^{3}H and ^{14}C labels included). After 10 min incubation at 37 °C, the reaction was initiated by adding *Hs*NAMPT to a final concentration of 230 nM. At 15−20% depletion of the substrate, 1400 μL of the reaction were quenched, and six 200 μL samples were loaded onto charcoal−cellulose columns (1:1 w/w, pre-equilibrated with water). The reaction product was then eluted with 1 mL of water and 5 mL of a 0.5 M solution of ammonium acetate (pH 6.6). The 100% depletion of NMN was achieved by adding extra PPi and enzyme (final concentration brought to 250 μM and 1.8 μM, respectively) to the 600 μL reaction volume. After completion, six 40 μL fractions were loaded onto similar columns as described above, following the same elution protocol. All samples (12 per independent experiment) were dried on a speed-vac, dissolved in 200 μL of water, and mixed with 12 mL of scintillation fluid (Ultima Gold, PerkinElmer), and their ^{3}H/^{14}C ratios were measured by scintillation counting (30 min/cycle, 10 cycles; dual-channel detector, Wallac 1414 LSC, PerkinElmer) after deconvolution of both channels. The channels 1 and 2 were set to have all ^{3}H signal (>99.9%) in channel 1, whereas counts in channel 2 arise only from ^{14}C; after calibration of the ratio (β) between those two channels using a source of ^{14}C ($>1 \times 10^5$ cpm), the exact amount of ^{3}H and ^{14}C in each of the samples was determined by the following relationships:

dx.doi.org/10.1021/ja310180c | J. Am. Chem. Soc. 2013, 135, 3485−3493

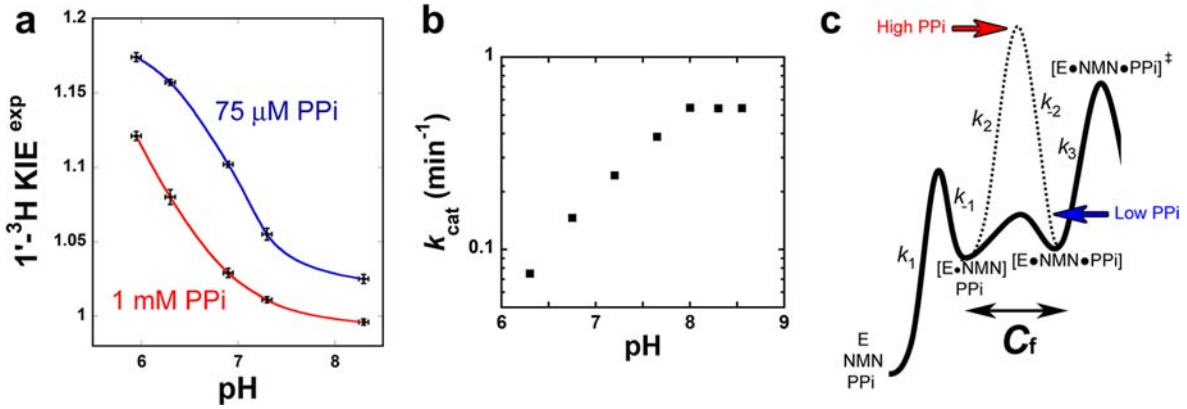

Figure 3. Influence of pH and PPi concentration on the experimental [1′-^{3}H] KIE. (a) Experimental [1′-^{3}H] KIEs were measured at high and low concentrations of PPi (1 mM and 75 μM, red and blue fits, respectively). For each set, a pH dependence profile was also established. Each data point is representative of one single experiment (see Matrials and Methods); the error bars for KIEs are the corresponding standard errors. Plots were made using KaleidaGraph 3.6 (Synergy Software). (b) Evaluation of k_{cat} upon pH variation. (c) Qualitative representation of the PPi concentration effect on forward commitment (C_f). At low PPi concentration, on this hypothetical reaction coordinate diagram, the transition state [E·^{14}C-NMN·PPi]‡ bears the highest energy barrier (step 3, $k_3 < k_{-2}$; plain trace); in this case, the KIEs will be close to intrinsic values. At high PPi concentration (dash trace), after crossing the higher barrier on step 2, the Michaelis complex evolves toward product formation. In this case, the experimental KIE will be reduced.

$$\mathrm{cpm}_{(^3\mathrm{H})} = \mathrm{cpm}_{(\mathrm{channel1})} - \mathrm{cpm}_{(\mathrm{channel2})}\beta$$
$$\mathrm{cpm}_{(^{14}\mathrm{C})} = \mathrm{cpm}_{(\mathrm{channel2})}(1 + \beta)$$

The corresponding ^{3}H/^{14}C ratios (R) for the partial (~20%, R_f) and complete (100%, R_0) conversion were used to correct the KIEs to 0% depletion of substrate:

$$\mathrm{KIE}_{\mathrm{obs}} = \frac{\ln(1-f)}{\ln\left(1 - f\frac{R_f}{R_0}\right)} \quad (1)$$

Measurements of Commitment Factors C_f and C_r. The external reverse commitment factor (C_r) for the *Hs*NAMPT-catalyzed reaction was evaluated under conditions where the NMN pyrophosphorolysis was irreversible. Because nicotinic acid is not a NAMPT substrate,[19] the [1′-^{3}H] KIE was measured following the same procedure as above, but in the presence of an excess of nicotinamidase. The forward commitment factor (C_f) to catalysis was measured by isotope trapping using rapid-mix pre-steady-state conditions.[27] NAMPT (50 μM) was incubated at 37 °C with [5′-^{3}H]NMN (175 μM; 5 × 10^6 cpm for 100 μL total final volume) in 50 mM MES (pH 6.30), 100 mM KCl, 5 mM $MgCl_2$, and 1 mM THP. A chase solution (7920 μL; 50 mM MES pH 6.30, 100 mM KCl, 5 mM $MgCl_2$, 1 mM THP, 1 mM unlabeled NMN, and 75 μM PPi), pre-equilibrated at 37 °C, was rapidly added to 80 μL of the above radioactive solution. Samples (1 mL, for four aliquots of 200 μL each) were quenched at the indicated time (Figure 4c) and quantified for product formation (α-D-5-phosphoribosyl-1-pyrophosphate (PRPP) elution on charcoal−cellulose columns as described above). Five replicates of this experiment were done. Background correction used the same experiment without enzyme. The concentration of labeled PRPP formed following addition of the chase solution was plotted as a function of the time (Figure 4c). As described in eq 2, extrapolation of this concentration to zero time allows determination of the fraction of product formed (PRPP) versus bound NMN (E·^{14}C-NMN) following dilution in excess of unlabeled NMN (cf. NMN K_d determination; Figure 4a; Supporting Information). After correction for forward commitment (eqs 3 and 4), the intrinsic KIEs were suitable for the computational chemistry study.

$$Y = \frac{[\mathrm{PRPP}]}{[\mathrm{E}\cdot^{14}\mathrm{C\text{-}NMN}]} \quad (2)$$

$$C_f = \frac{Y}{1-Y} \quad (3)$$

$$\mathrm{KIE} = \mathrm{KIE}_{\mathrm{exp}}(1 + C_f) - C_f \quad (4)$$

Computational Modeling of Transition-State Structure. A previously published crystal structure of NAMPT, with bound NMN and Mg_2PPi (PDB: 3DHD), was used as the starting point for the calculations.[20] Each of the calculated transition structures is characterized by only one imaginary frequency corresponding to reaction coordinate motion. KIEs for these transition structures are computed using ISOEFF98,[28,29] and a one-dimensional infinite parabola correction is applied to account for tunneling contributions to the KIEs.[30] The ESPSs were calculated by using the CUBE program from Gaussian 09.[31] Checkpoints files for CUBE inputs were generated at B3LYP/6-31G* for the optimized geometries at the same level of theory and visualized with GaussView 3.0.

Reactivity of 5P-pNR against NAMPT and Inhibition Properties. Reactivity assay was performed in TRIS buffer (50 mM, pH 8.0) supplied with 1 mM PPi, 5 mM $MgCl_2$, and 100 μM 5′-phospho-*p*-nitrophenyl-β-D-ribofuranoside (5P-pNR). The reaction started by addition of NAMPT (10 μM final concentration). Signal was monitored at 430 nm and compared against a control sample (same as above without NAMPT). Possible inhibition of the NMN pyrophosphorolysis by 5P-pNR was assessed by monitoring the initial reaction rates at various 5P-pNR concentrations (5−100 μM) using 20 μM [5′-^{3}H]NMN, 1 mM PPi, 5 mM $MgCl_2$, and 90 nM NAMPT (50 mM HEPES, pH 7.5). Radiolabeled product was isolated by solid-phase extraction, and radioactivity was quantified by scintillation counting. Correlation between initial velocities and the corresponding inhibitor concentrations allows determination of the K_i.

RESULTS

Experimental KIEs Are Suppressed under Typical Experimental Conditions. Intrinsic KIEs are required for the interpretation of enzymatic TSs.[32] The [1′-^{3}H] label was used to evaluate the extent of KIE suppression as a function of experimental conditions. The [1′-^{3}H] position is alpha to the *N*-ribosidic bond and is expected to display a significant KIE for the NMN pyrophosphorolysis reaction. Under optimum conditions for conversion of NMN to NAM (1 mM PPi, pH 7.30), this KIE is near unity (1.011 ± 0.002; Figure 3a). Although *Hs*NAMPT activity is restricted to a narrow pH

dx.doi.org/10.1021/ja310180c | J. Am. Chem. Soc. 2013, 135, 3485−3493

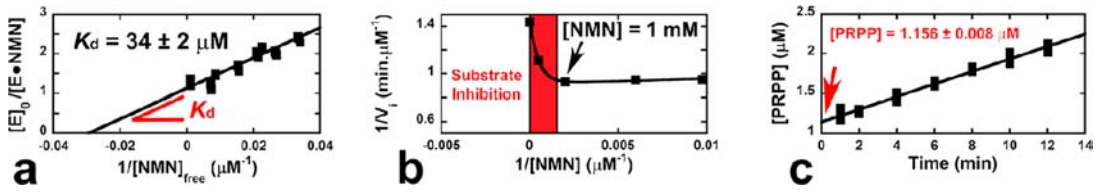

Figure 4. Determination of the forward commitment factor (C_f) by isotope trapping for the pyrophosphorolysis of NMN catalyzed by *Hs*NAMPT. (a) Determination of the NMN dissociation constant at 37 °C and pH 6.30 (MES). The dissociation constant between NMN and NAMPT (K_d = 34 ± 2 μM) allows determination of the E·NMN complex concentration (by mixing 50 μM of enzyme with 175 μM of radioactive NMN, the E·NMN complex concentration becomes equal to 39.95 μM; Supporting Information). (b) The NMN substrate inhibition. The isotope trapping method, used to determine C_f, is performed at high concentration of NMN, yet this method is irrelevant in the presence of a substrate inhibition (red zone). Here, a 1 mM NMN concentration is still suitable (Supporting Information). (c) Isotope trapping experiment. The synthesis of PRPP is monitored over time. After extrapolation to the origin ([PRPP] = 1.156 ± 0.008 μM), eqs 2−4 allow determination of the C_f value (Y = 1.156/39.95 = 0.0289 and C_f = 0.0298 ± 0.0003; see Materials and Methods). Plots were made with KaleidaGraph 3.6 (Synergy Software).

range,[21] the [1′-^{3}H] KIE at pH values between 8.30 and 5.95 (Figure 3a) revealed that acidic conditions contribute to better expression of the experimental KIE (Figure 3a). Indeed, NAMPT reveals a pH dependence for k_{cat} (Figure 3b), while K_m is almost constant (1−2 μM). Acidic pH (6.30) decreases k_{cat}/K_m by a factor of 15, consistent with the improved expression of KIEs.

Reducing the PPi concentration to 75 μM also increased the isotope effect, and at the lowest pH, the experimental KIE value approaches the upper limit of an intrinsic KIE calculated for this position (Figure 3a). Increased PPi concentration affects the KIEs of this bisubstrate reaction by increased forward commitment factors.[33] At high PPi concentrations, the KIEs are abolished. At low PPi concentrations, the isotope effects tend to their intrinsic values (Figure 3c). These observations are reminiscent of results previously obtained with orotate phosphoribosyltransferase, another PPi-dependent *N*-ribosyl transferase. The use of natural substrates (i.e., orotidine 5′-monophosphate and PPi) abrogates KIE expression at physiological pH; it is only when the slow substrate analogue phosphonoacetic acid is used that the KIEs can be measured.[34] Hence, experimental conditions were varied to reduce the commitment factors and allow determination of KIEs close to their intrinsic values. Optimum KIEs were observed at 37 °C, pH 6.30, and in the presence of 75 μM PPi.

Forward and Reverse Commitment Factors (C_f and C_r). Commitment factors obscure intrinsic KIEs and only the intrinsic KIEs are useful in defining TS structure. Intrinsic KIEs are therefore required for TS determination. Observed, experimental KIEs can be corrected to intrinsic KIEs by determination of kinetic commitment factors.

The forward commitment factor (C_f) reflects the probability of the Michaelis complex [E·^{14}C-NMN·PPi] to dissociate to unreacted substrates relative to generating products (i.e., $C_f = k_{cat}/k_{off}$, where k_{cat} and k_{off} are equivalent to k_3 and k_{-2}, respectively; Figure 3c). We determined C_f by the isotope-trapping method of Rose.[27] From a 40 μM preformed [E·^{14}C-NMN] complex (K_d = 32 μM; Figure 4a), a rapid-mix dilution into excess NMN (i.e., 1 mM; Figure 4b) and 75 μM PPi allowed the monitoring of radiolabeled PRPP formation (Figure 4c). With those conditions, only 2.89% of the initial [E·^{14}C-NMN] complex is converted to product (1.156 μM PRPP; Figure 4c). The corresponding C_f is 0.0298 (eqs 2 and 3, Figure 4c).

Isotope trapping may also be applied to the determination of reverse commitment, the ability of enzyme-bound products to re-form the enzyme-bound substrates before product release. However, the chemical instability of PRPP makes this experiment technically challenging. Instead, we measured the [1′-^{3}H] KIE under conditions where NMN pyrophosphorolysis is made externally irreversible by hydrolysis of NMN with excess nicotinamidase. When using nicotinamidase, the experimental KIE was 1.148 ± 0.002 (SD = 0.022), compared to 1.161 ± 0.002 (SD = 0.019) in the absence of the deaminase. Although these results are statistically different (t test, t = 8.85 and $p < 0.001$), a lower KIE value obtained with nicotinamidase precludes significant C_r. Thus, the [1′-^{3}H] KIE was averaged to 1.154 (Table 1).

Intrinsic KIEs and Their Significance. Intrinsic KIEs for atoms near the reaction center report on the nature of the TS. The isotope effect from [5′-^{14}C]NMN is three bonds away from the reaction center and is assumed to be unity. The [1-^{15}N]NMN and [1′-^{14}C]NMN experimental KIEs were corrected for their [5′-^{3}H] control labels using eq 5. The contributions from forward and reverse commitment are small and the experimental and intrinsic KIEs were within experimental error (Table 1).

$$KIE_{exp} = KIE_{obs}KIE^{(5'^3Hor4'-^3H)} \quad (5)$$

The KIE for the C1′ position is sensitive to atomic motion along the reaction coordinate and reflects the interactions of the leaving group (NAM) and nucleophile (PPi) with the anomeric carbon at the TS. This KIE is often critical for defining the reaction mechanism (e.g., S_N1 vs S_N2).[35] The 1.047 primary [1′-^{14}C]NMN isotope effect for NMN pyrophosphorolysis suggests significant nucleophilic involvement at the TS. The accompanying large [1-^{15}N]NMN isotope effect is consistent with full C−N bond cleavage at the TS.

The α-secondary [1′-^{3}H] KIE reflects an increase in the out-of-plane C1′−H1′ bending mode as C1′ rehybridizes from sp^3 to sp^2. Large KIEs (>1.250) at this position are characteristic of steric freedom for the C1′−H bond at the TS relative to substrate, with a limited participation of both nucleophile and leaving group (i.e., highly developed oxacarbenium).[36] We measured a 1.154 KIE for the H1′ position, consistent with weak residual bond order to C1′ at the TS (Table 1).

We used [2′-^{3}H]NMN and detected a β-secondary KIE of 1.093. The magnitude of this effect provides information about the ribosyl geometry at the TS, where a large KIE is characteristic of maximum hyperconjugation between the C2′−H2′ σ bond and the 2p$_z$ orbital of the anomeric carbon (C1′) at the TS.[37] Although this position is crucial to determine the TS geometry, a direct interpretation requires computational chemistry (see below).

dx.doi.org/10.1021/ja310180c | J. Am. Chem. Soc. 2013, 135, 3485−3493

Table 1. Intrinsic and Calculated KIEs for the Pyrophosphorolysis of NMN Catalyzed by *Hs*NAMPT

substrate	type of KIE	intrinsic KIEs[a]		calculated KIEs	
[1-^{15}N, 5′-^{14}C]NMN	primary ^{15}N	1.029 ± 0.002[b]	(8; ± 0.003)[c]	1.024[d]	1.024[e]
[1′-^{14}C]NMN	primary ^{14}C	1.047 ± 0.002	(8; ± 0.004)	1.043	1.046
[1′-^{3}H]NMN	α-secondary ^{3}H	1.154 ± 0.001	(8; ± 0.003)	1.154	1.163
[2′-^{3}H]NMN	β-secondary ^{3}H	1.093 ± 0.001	(4; ± 0.003)	1.142	1.090
[4′-^{3}H]NMN	γ-secondary ^{3}H	0.998 ± 0.001	(4; ± 0.003)	–	
[5′-^{3}H]NMN	δ-secondary ^{3}H	1.019 ± 0.001	(4; ± 0.004)	–	

[a]Experimental KIEs have been previously corrected to 0% substrate depletion using eq 1. Intrinsic KIEs were obtained by correction of the observed KIEs for remote ^{3}H label and for forward commitment factor (C_f = 0.0298 ± 0.0003; Figure 4) using eqs 2–4. [b]Each intrinsic KIE is provided with its standard error; standard errors less than 0.001 were rounded-up to 0.001. [c]The numbers in parentheses are the number of independent experiments and the 95% confidence intervals, respectively. Each independent experiment is composed of six samples for 20% substrate depletion and six samples for 100% substrate depletion, which by combination provide a total of 36 KIEs. [d]Theoretical KIEs were determined on the final TS model from Figure 5a using B3LYP/6-31G* gas-phase calculations (see Materials and Methods). [e]Theoretical KIEs were determined on the final TS (r_{C-O} = 2.60 Å, r_{C-N} = 2.35 Å) using B3LYP(PCM:diethyl ether)/6-31G* calculations (see Materials and Methods); remote 5′- and 4′-positions are used only as remote labels and were not included in the analysis.

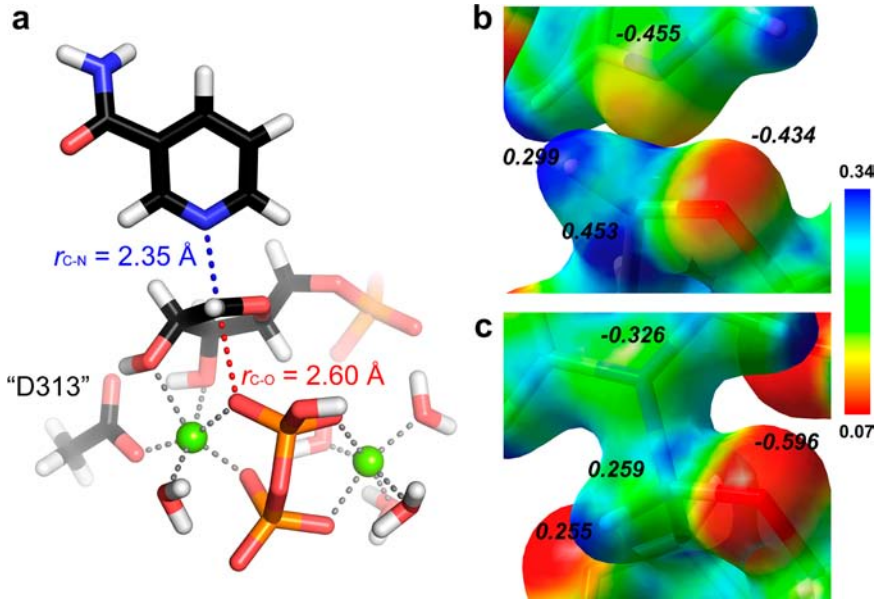

Figure 5. TS of *Hs*NAMPT—geometry and characteristics. (a) Geometry of the transition state matching the intrinsic KIEs. The C1′-nucleophile (r_{C-O}) and the C1′-leaving group (r_{C-N}) distances are depicted in red and blue dashed lines, respectively. Also represented, and incorporated in the computational model, are magnesium atoms (green balls) and their corresponding ligands (gray dashed lines). (b) Close-up on the electrostatic potential surface (ESPS) of the TS, at the C1′ vicinity. (c) Close-up on the ESPS of the NMN reactant state, at the C1′ vicinity. ESPSs were calculated at B3LYP/6-31G* for the optimized geometries at the same level of theory and visualized with GaussView 3.0 (Supporting Information); blue coloring corresponds to a relative electron deficiency, while red defines a relative electron enrichment (see color coding and its arbitrary scaling units). The natural charges from NBO calculations for O4′, C1′, H1′, and N1 atoms are also represented (in italics).

The tritium isotope effects at the 5′- and 4′-position were determined for remote control purposes. These two positions are not considered in the determination of the final TS geometry (Table 1).

Modeling the *Hs*NAMPT TS. A TS model consistent with the intrinsic KIEs for pyrophosphorolysis of NMN was determined in B3LYP/6-31G* calculations[38] as implemented in Gaussian 09. The TS model includes unmodified substrates NMN and PPi, two Mg^{2+} ions critical to the reaction, and five water molecules. Also included is a chemical mimic of an active site aspartate (D313), which along with PPi, complete the octahedral coordination of both Mg^{2+} ions (Figure 5a).[20] A series of TSs were located by fixing the two key distances along the reaction coordinate, i.e., the forming C–O bond (r_{C-O}) and the breaking C–N (r_{C-N}) bond, with no additional restraints placed on other parameters (Supporting Information). To better simulate the enzyme active site, the geometry that gave the best fit to the experimental KIEs in the gas-phase calculations was recalculated using a polarizable continuum model (PCM) with three different solvents: diethyl ether, acetone, and water (with increasing dielectric constants of 4.24, 20.49, and 78.36, respectively). Inclusion of a solvent model had a significant impact on the accurate prediction of the [2′-^{3}H] KIE but did not significantly alter the heavy-atom KIE predictions (Table 1). The closest match to experimental KIEs was obtained with the B3LYP(PCM:diethyl ether)/6-31G* calculations. A low dielectric constant (diethyl ether) is often used for PCM calculations when modeling of a protein environment is desired.[39,40]

The TS that best matches the intrinsic KIEs for the *Hs*NAMPT-catalyzed reaction exhibits a minimal bond order to the attacking PPi nucleophile (r_{C-O} = 2.60 Å) and weak but significant bond order to the leaving group (r_{C-N} = 2.35 Å; Table 1 and Figure 5a). There is significant ribocation character

dx.doi.org/10.1021/ja310180c | J. Am. Chem. Soc. 2013, 135, 3485–3493

at the TS, akin to other *N*-ribosyltransferases (Figure 5b,c).[41] We performed a charge analysis of the TS relative to the ground state (Figure 5b,c). Though NMN is often depicted with a positive charge "+" on its nitrogen, the positive charge of NMN resides primarily on the anomeric carbon in the ground state, as evidenced by the +0.259 natural charge on C1′ and the −0.326 natural charge on N1. As the C1′−N1 bond strength decreases at the TS, increased electron density appears on N1 (Figure 5b). The development of ribocation character at the TS is supported by the decreased electron density on O4′ (natural charge increasing from −0.596 to −0.434) and the sustained electron deficiency on C1′ (Figure 5b). The presence of the attacking oxygen atom from PPi (at 2.60 Å from C1′) has an electrostatic contribution to the net charge of C1′, even though there is no significant bond order to this oxygen atom. [NBO analysis of the TS with identical r_{C-N} but without the attacking nucleophile showed an increased positive charge at C1′ when compared to NMN.]

The pucker of the ribose ring is governed by its contacts with D313 and one of the active site Mg^{2+} ions. The D313($O\delta_2$) forms hydrogen bonds to the hydroxyl protons from O2′ and O3′ and the Mg^{2+} ion coordinates with the same O2′ and O3′ atoms (Figure 5a). The coordination of the same Mg^{2+} ion to D313($O\delta_1$) increases the rigidity of the ribose ring, thus enforcing a "flat" geometry at the TS. The other Mg^{2+} ion is coordinated to two oxygen atoms of PPi and four water molecules, two of which interact with the 5′-phosphate moiety through hydrogen bonding.

Considering that the transition structure in Figure 5a was constrained *only* along the reaction coordinate and was relaxed in all other dimensions, the agreement of experimental and predicted KIEs is remarkable (Table 1). Shown in Table 1 is a comparison of the experimental KIEs and the KIE predictions for the TS geometry in Figure 5a (for both gas-phase and PCM (diethyl ether) structures). The predicted KIEs at the reaction center, i.e., [1′-^{14}C], [1′-^{3}H], and [1-^{15}N] KIEs, are in close agreement to intrinsic KIEs values in both gas-phase and PCM calculations. The [2′-^{3}H] KIE, which reports on the ribose ring pucker, is usually challenging to predict without restraining the H2′−C2′−C1′−H1′ dihedral angle. Since our model includes the active site elements that determine the ring pucker (namely the aspartate mimic and one of the Mg^{2+} ions), we expected to obtain a good match for the [2′-^{3}H] KIE even without restricting the H2′−C2′−C1′−H1′ dihedral angle. Our gas-phase model slightly over-predicts the [2′-^{3}H] KIE (1.142); however, inclusion of a PCM model resulted in an excellent match of experiment (1.093 ± 0.003) and theory (1.090). We attribute this excellent match of theory and experiment to the detailed modeling of the chemically relevant active site environment with full substrates, Mg^{2+} ions and their ligands, as well as the use of a PCM (diethyl ether) to provide an accurate description of the catalytic site environment for *Hs*NAMPT. [A simpler model with only one Mg^{2+} ion and a 5′-deoxynicotinamide riboside was unable to simultaneously predict all the experimental KIEs (Figure S2).]

The slight discrepancy between experimental and predicted [1-^{15}N] KIE (1.029 vs 1.024; Table 1) might suggest to the reader that C−N bond-scission is slightly more advanced than 2.35 Å at the TS. Geometries with slightly extended r_{C-N} distances (up to 2.80 Å) and slightly shortened r_{C-N} distances (that still gave good match of the [1′-^{14}C] KIE) resulted in a slightly better ^{15}N KIE prediction of up to 1.026; however, the [1′-^{3}H] and [2′-^{3}H] KIE predictions for these geometries departed significantly from experiment (Supporting Information). The use of a higher level of theory with diffuse functions (B3LYP/6-31+G*) did not significantly improve the [1-^{15}N] KIE prediction (Supporting Information). While the predicted 1.024 ^{15}N KIE seems reasonably close to the experimental value of 1.029 (especially if one considers the corresponding 95% confidence interval of 0.003; Table 1), we believe that the slightly lower predicted ^{15}N KIE might be a result of not considering the environment around the leaving group in our model (e.g., π-stacking, H-bonding). Finally, in addition to the concerted bimolecular process (A_ND_N) described above, two stepwise mechanisms were also considered: (a) S_N1 mechanism with irreversible leaving group departure (the first step, $D_N{}^{\ddagger}{*}A_N$) and (b) S_N1 mechanism with irreversible nucleophilic attack (the second step, $D_N{*}A_N{}^{\ddagger}$). Both these possibilities were discounted based on the poor match of experimental and theoretical KIEs. (See Supporting Information for full details on these calculations.)

Leaving Group Activation in the NAMPT-Catalyzed Reaction. The 5P-pNR is an excellent probe to elucidate the mechanism by which NAMPT achieves its oxacarbenium ion TS. If the enzyme ionizes a ribosyl hydroxyl to facilitate the departure of NAM, or interacts with the ribosyl group of NMN to stabilize an oxacarbenium ion, the 5P-pNR is expected to be a good substrate for NAMPT; the departure of the *p*-nitrophenyl moiety does not need assistance from the enzyme (e.g., hydrogen bonds, protonation). On the other hand, if NAM activation is required to reach the TS, the 5P-pNR would be a poor substrate. The chemical mechanism by which NAMPT achieves its TS was analyzed in the presence of PPi (see Materials and Methods).[34] 5P-pNR was not a substrate for NAMPT under conditions that would have detected 10^{-4} of the rate relative to NMN. However, 5P-pNR was capable of binding to NAMPT to give K_i = 2.5 μM vs K_m^{NMN} = 0.74 μM. We conclude that leaving-group activation is the major force in reaching the TS for the NAMPT-catalyzed reaction.

DISCUSSION

Kinetic isotope effects provide the one experimental approach capable of providing atomic-level information of the TS geometry (bond distances, angles, and charges). Our results provide the most accurate representation of the reaction catalyzed by NAMPT.

Superimposition of the NAMPT crystal structures (NAMPT·NMN·Mg_2PPi and NAMPT·benzamide·PRPP, PDB: 3DHD and 3DKJ, respectively) supported a reaction mechanism of "nucleophilic displacement by electrophile migration".[20] According to our TS model, C1′ "migrates" 0.87 Å (C1′−N = 1.48 Å in NMN and 2.35 Å at the TS) from the leaving group NAM to reach the TS (residual bond order, n = 0.06). At the TS, the bond order to the nucleophile is low (n = 0.02), and C1′ is still 2.60 Å from the nucleophilic oxygen atom of PPi. An additional migration of 1.15 Å is required to complete the reaction coordinate and generate PRPP. The 2.0 Å excursion of C1′ from leaving group to nucleophile is close to the distance from the crystal structures cited above (2.2 Å). At the TS, the C1′−O4′ bond becomes significantly shorter (Δn = +0.65), and the C1′−N1 bond elongates (Δn = −0.85).These atomic modifications cause accumulation of negative charge on the NAM ring. A decreased natural charge on the nitrogen atom (Δ = −0.129) matches the formation of a positive charge on the ribosyl ring (Figure 5). The extra positive charge on C1′ (Δ = +0.194) justifies the term "ribooxacarbenium ion".

dx.doi.org/10.1021/ja310180c | J. Am. Chem. Soc. 2013, 135, 3485−3493

Enzymes exclude competitive nucleophiles (i.e., water) from their active sites to promote an efficient substrate/product transformation during catalysis. With NAMPT, the vicinity of C1′ is water-free except for WAT532 positioned 3.7 Å from the reactive center (PDB: 3DHD). Free water diffuses at 1 Å ps^{-1}, and it would take approximately 2 ps for an unfettered water at this position to diffuse and react with the ribocation. However, this structural water participates in hydrogen bonding with Y*18(OH, from the neighboring subunit) and R311($N\eta_1$) at 2.7 and 3.2 Å, respectively, precluding water diffusion and reaction with the ribocation. In human purine nucleoside phosphorylase, a chemistry-related *N*-ribosyltransferase, atomic motion constituting the reaction coordinate is complete in under 100 fs, faster than diffusion times for even closer waters.[42]

NAMPT's active site imposes constraints on atomic motions to promote trajectories that would be less probable in solution chemistry. When comparing NMN hydrolysis (k = 1.04 ± 0.01 × 10^{-3} h^{-1}; Figure S3a) to the enzyme-catalyzed NMN pyrophosphorolysis (k_{cat} = 0.48 ± 0.01 min^{-1}; Figure S3b), we estimate that this reaction is improved 30 000-fold by NAMPT. This modest rate enhancement (ξ; Figure S3) emphasizes the chemical instability of the *N*-ribosidic bond in NMN. Rate enhancement occurs by stabilization of the ribocation through electrostatic interactions and by charge delocalization from the ribose ring through hydrogen bonds as proposed for diphtheria toxin (DT).[43]

Enzymes with nicotinamide *N*-ribosyltransferase activities similar to that of NAMPT include DT and sirtuins. X-ray analysis and molecular dynamics studies of DT revealed the crucial role of Glu148 forming a hydrogen bond to the 2′-OH in both enzyme−substrate and enzyme−TS complexes.[44,45] This interaction causes charge delocalization in both ground state and TS to facilitate formation of a ribooxocarbenium ion at the TS. Ionization of the 2′-OH in solution (i.e., NAD and nicotinamide riboside) would facilitate the NAM−ribosyl bond hydrolysis at a rate 10 000-fold that for a fully protonated 2′-OH.[46] Despite the stabilization of the ribocation near the TS, the reaction is initiated by leaving-group interactions with the NAM, since *p*-nitrophenyl-β-D-riboside would be a good substrate if reaction initiation occurred via formation of a ribocation.[47]

Other phosphoribosyl transferases (PRTases) also place aspartatic and/or glutamic residues in the O2′ and O3′ vicinity (e.g., hypoxanthine/guanine/xanthine, adenine, and orotate PRTases, Figure S4). Although the position of these conserved residues among PRTases is similar to that in NAMPT structures, the binding modes for substrates and Mg^{2+} are very different. NAMPT always contains two structural Mg^{2+} ions and NAMPT D313 coordinates with a bound magnesium ion. The aspartic or glutamic moieties from other PRTases are part of the second coordination sphere and the 2′- and/or 3′-hydroxyls from the respective ribosyl substrates (Figure S4). According to our calculations, the natural charge at O2′ is −0.779 and −0.797 for NMN and the TS, respectively; such a variation precludes a D313-mediated ionization. Instead, D313 may form a favorable hydrogen bond with NMN (distance $O\delta_2$−O3′ being 2.5 Å; PDB: 3DHD). Its main role in catalysis might be limited to Mg^{2+} coordination for optimal conformation of substrates (cf. computational model; Figure 5a).

Leaving-group activation (for NAM) is a major driving force in the NAMPT reaction, similar to recent results with OPRTase.[48] Unlike related PRTases (APRTase or HGXPRTase), where protonation/deprotonation of the purine ring is ensured by acid/base catalysis (Figure S4), hydrogen bonding from Arg311($N\varepsilon$)−O_{amide} (3.1 Å) and Asp($O\delta_2$)−N_{amide} (3.2 Å) to NAM provides sufficient stabilization and electrostatic interactions from π-stacking with Phe193/Tyr*18 to activate the leaving group.

The TS from NAMPT is concerted: the residual bond order to the leaving group is 0.06, and the bond order to the approaching nucleophile is 0.02 (Table 2). Our TS shares similarities with the TS from the NAD hydrolysis catalyzed by DT.[49] Although both reactions follow an A_ND_N mechanism, the *N*-ribosidic bond is elongated to a greater extent for the DT-catalyzed hydrolysis (Table 2). In both cases, the approaching nucleophile weakly interacts (n = 0.02−0.03; Table 2). This characteristic is very distinct from the NAD hydrolysis catalyzed by Pertussis toxin where participation of the water nucleophile is weak (S_N1 reaction, n = 0.001, r_{C-O} > 3.5 Å; Table 2).[50] Finally, when compared to the ADP-ribosylations catalyzed by DT and PT toxins, the pyrophosphorolysis of NMN is more concerted. Although the r_{C-Nu} distances are quite similar (~2.50−2.60 Å), the loss in bond order of the NAM leaving group is more substantial for the NAMPT catalyzed reaction (n = 0.06; Table 2) than it is for the ADP-ribosylation of eEF-2 catalyzed by DT (n = 0.18; Table 2).[43,51,52]

Table 2. Bond Order and Bond Length at the Transition State of the NMN Pyrophosphorolysis Catalyzed by *Hs*NAMPT and Comparison with Other Reactions Catalyzed by NAD-Utilizing Enzymes

	r_{C-LG} (r_{C-N})		r_{C-Nu} (r_{C-X})[a]	
system	bond order[b]	bond length, Å	bond order	bond length, Å
DT NAD hydrolysis (O)[a]	0.02	2.65	0.03	2.46
NAMPT NMN PPi (O)	**0.06**	**2.35**	**0.02**	**2.60**
PT NAD hydrolysis (O)	0.11	2.14	0.001	3.50
PT NAD $G_{i\alpha1}$ (S)	0.13	2.10	0.09	2.55
PT NAD $_{\alpha i3}$C20 (S)	0.15	2.06	0.12	2.47
DT NAD eEF-2 (N)	0.18	1.99	0.03	2.58

[a]The nature of the atom nucleophile depends on the system studied. It is an oxygen atom for the NAD hydrolysis catalyzed by both diphtheria and pertussis toxins (DT and PT, respectively) or for the pyrophosphorolysis of NMN catalyzed by NAMPT. It is a sulfur atom for the ADP-ribosylation of $G_{i\alpha1}$ and α_{i3}C20 peptides by PT toxin. Finally, it is a nitrogen atom when the DT toxin ADP-ribosylates eukaryotic elongation factor 2 (eEF-2). [b]Pauling bond orders are calculated using the relation $n_i = e^{(r-r_i)/0.3}$, where r is the bond length of a single bond (i.e., r_{C-N} = 1.48 Å, r_{C-S} = 1.83 Å, r_{C-O} = 1.44 Å) and r_i is the interatomic distance between C1′ and the atom of interest (i.e., r_{C-LG} and r_{C-Nu}).

CONCLUSIONS

Intrinsic KIEs were measured with pyrophosphate as the nucleophile in the NAMPT reaction. By incorporating structural elements from the catalytic site into the quantum chemical calculations, an unbiased TS structure was located to match the intrinsic KIEs. This unique computational approach will be useful in TS analysis of other enzymes, especially those involving pyrophosphorolysis. A ribosyl carbocation develops at the TS surrounded by nicotinamide and pyrophosphate, 2.35 and 2.60 Å away from the anomeric C1′, respectively. Determination of the TS features permits the creation of an

dx.doi.org/10.1021/ja310180c | J. Am. Chem. Soc. 2013, 135, 3485−3493

electrostatic potential surface that may assist in the design of TS analogues for NAMPT.

■ ASSOCIATED CONTENT

Supporting Information

Supporting Materials and Methods, including the synthesis of labeled substrates (^{15}N, ^{14}C, and ^{3}H), the dissociation constant (K_d) for NMN onto *Hs*NAMPT and the substrate inhibition experiment, description of computational methodology, and corresponding coordinates of calculated structures; Figure S1, synthesis of radiolabeled NMN; Figure S2, first approach to solve *Hs*NAMPT TS by computational chemistry using 5′-deoxy-nicotinamide riboside, MgPPi, and acetic acid; Figure S3, determination of ξ for *Hs*NAMPT; Figure S4, comparison of catalytic features of a few PRTases. This material is available free of charge via the Internet at http://pubs.acs.org.

■ AUTHOR INFORMATION

Corresponding Author

vern.schramm@einstein.yu.edu

Notes

The authors declare no competing financial interest.

■ ACKNOWLEDGMENTS

We thank P. C. Tyler of Industrial Research Laboratory, Inc. for supplying the 5P-pNR, S. L. Mowbray (Swedish University of Agricultural Sciences, Uppsala, Sweden) for providing *E. coli* ribokinase, J. C. Escalante-Semerena (University of Wisconsin, Madison) for the *S. enterica* PncA nicotinamidase, and the U.S. National Institutes of Health grant GM41916 for funding.

■ REFERENCES

(1) Corda, D.; Di Girolamo, M. *EMBO J.* **2003**, *22*, 1953.
(2) Menissier de Murcia, J.; Ricoul, M.; Tartier, L.; Niedergang, C.; Huber, A.; Dantzer, F.; Schreiber, V.; Ame, J. C.; Dierich, A.; LeMeur, M.; Sabatier, L.; Chambon, P.; de Murcia, G. *EMBO J.* **2003**, *22*, 2255.
(3) Blander, G.; Guarente, L. *Annu. Rev. Biochem.* **2004**, *73*, 417.
(4) Sauve, A. A.; Wolberger, C.; Schramm, V. L.; Boeke, J. D. *Annu. Rev. Biochem.* **2006**, *75*, 435.
(5) van der Veer, E.; Ho, C.; O'Neil, C.; Barbosa, N.; Scott, R.; Cregan, S. P.; Pickering, J. G. *J. Biol. Chem.* **2007**, *282*, 10841.
(6) Brunet, A.; Sweeney, L. B.; Sturgill, J. F.; Chua, K. F.; Greer, P. L.; Lin, Y.; Tran, H.; Ross, S. E.; Mostoslavsky, R.; Cohen, H. Y.; Hu, L. S.; Cheng, H. L.; Jedrychowski, M. P.; Gygi, S. P.; Sinclair, D. A.; Alt, F. W.; Greenberg, M. E. *Science* **2004**, *303*, 2011.
(7) Vaziri, H.; Dessain, S. K.; Ng Eaton, E.; Imai, S. I.; Frye, R. A.; Pandita, T. K.; Guarente, L.; Weinberg, R. A. *Cell* **2001**, *107*, 149.
(8) Schriner, S. E.; Linford, N. J.; Martin, G. M.; Treuting, P.; Ogburn, C. E.; Emond, M.; Coskun, P. E.; Ladiges, W.; Wolf, N.; Van Remmen, H.; Wallace, D. C.; Rabinovitch, P. S. *Science* **2005**, *308*, 1909.
(9) Mitsui, A.; Hamuro, J.; Nakamura, H.; Kondo, N.; Hirabayashi, Y.; Ishizaki-Koizumi, S.; Hirakawa, T.; Inoue, T.; Yodoi, J. *Antioxid. Redox Signal.* **2002**, *4*, 693.
(10) Graeff, R.; Liu, Q.; Kriksunov, I. A.; Kotaka, M.; Oppenheimer, N.; Hoa, Q.; Lee, H. C. *J. Biol. Chem.* **2009**, *284*, 27629.
(11) Burgos, E. S. *Curr. Med. Chem.* **2011**, *18*, 1947.
(12) Revollo, J. R.; Grimm, A. A.; Imai, S. *J. Biol. Chem.* **2004**, *279*, 50754.
(13) Jia, S. H.; Li, Y.; Parodo, J.; Kapus, A.; Fan, L.; Rotstein, O. D.; Marshall, J. C. *J. Clin. Invest.* **2004**, *113*, 1318.
(14) Van Beijnum, J. R.; Moerkerk, P. T.; Gerbers, A. J.; De Bruine, A. P.; Arends, J. W.; Hoogenboom, H. R.; Hufton, S. E. *Int. J. Cancer* **2002**, *101*, 118.
(15) Bae, Y. H.; Bae, M. K.; Kim, S. R.; Lee, J. H.; Wee, H. J.; Bae, S. K. *Biochem. Biophys. Res. Commun.* **2009**, *379*, 206.
(16) Bauer, L.; Venz, S.; Junker, H.; Brandt, R.; Radons, J. *Int. J. Oncol.* **2009**, *35*, 97.
(17) Wang, B.; Hasan, M. K.; Alvarado, E.; Yuan, H.; Wu, H.; Chen, W. Y. *Oncogene* **2011**, *30*, 907.
(18) Hasmann, M.; Schemainda, I. *Cancer Res.* **2003**, *63*, 7436.
(19) Khan, J. A.; Tao, X.; Tong, L. *Nat. Struct. Mol. Biol.* **2006**, *13*, 582.
(20) Burgos, E. S.; Ho, M. C.; Almo, S. C.; Schramm, V. L. *Proc. Natl. Acad. Sci. U.S.A.* **2009**, *106*, 13748.
(21) Burgos, E. S.; Schramm, V. L. *Biochemistry* **2008**, *47*, 11086.
(22) Watson, M.; Roulston, A.; Belec, L.; Billot, X.; Marcellus, R.; Bedard, D.; Bernier, C.; Branchaud, S.; Chan, H.; Dairi, K.; Gilbert, K.; Goulet, D.; Gratton, M. O.; Isakau, H.; Jang, A.; Khadir, A.; Koch, E.; Lavoie, M.; Lawless, M.; Nguyen, M.; Paquette, D.; Turcotte, E.; Berger, A.; Mitchell, M.; Shore, G. C.; Beauparlant, P. *Mol. Cell. Biol.* **2009**, *29*, 5872.
(23) Olesen, U. H.; Petersen, J. G.; Garten, A.; Kiess, W.; Yoshino, J.; Imai, S.; Christensen, M. K.; Fristrup, P.; Thougaard, A. V.; Bjorkling, F.; Jensen, P. B.; Nielsen, S. J.; Sehested, M. *BMC Cancer* **2010**, *10*, 677.
(24) Andersson, C. E.; Mowbray, S. L. *J. Mol. Biol.* **2002**, *315*, 409.
(25) Garrity, J.; Gardner, J. G.; Hawse, W.; Wolberger, C.; Escalante-Semerena, J. C. *J. Biol. Chem.* **2007**, *282*, 30239.
(26) Parkin, D. W. In *Enzyme mechanism from isotope effects*; Cook, P. F., Ed.; CRC Press, Inc.: Boca Raton, FL *33431*, 1991; p 269.
(27) Rose, I. A. *Methods Enzymol.* **1980**, *64*, 47.
(28) Anisimov, V.; Paneth, P. *J. Math. Chem.* **1999**, *26*, 75.
(29) Frequencies were scaled by 0.9614; Scott, A. P.; Radom, L. *J. Phys. Chem.* **1996**, *100*, 16502.
(30) Bell, R. P. *The tunnel effect in chemistry*; Chapman & Hall: London, 1980.
(31) Frisch, M. J.; Trucks, G. W.; Schlegel, H. B.; Scuseria, G. E.; Robb, M. A.; Cheeseman, J. R.; Scalmani, G.; Barone, V.; Mennucci, B.; Petersson, G. A.; Nakatsuji, H.; Caricato, M.; Li, X.; Hratchian, H. P.; Izmaylov, A. F.; Bloino, J.; Zheng, G.; Sonnenberg, J. L.; Hada, M.; Ehara, M.; Toyota, K.; Fukuda, R.; Hasegawa, J.; Ishida, M.; Nakajima, T. E.; Honda, Y.; Kitao, O.; Nakai, H.; Vreven, T.; Montgomery, J. A.; Peralta, J. E.; Ogliaro, F.; Bearpark, M.; Heyd, J. J.; Brothers, E.; Kudin, K. N.; Staroverov, V. N.; Kobayashi, R.; Normand, J.; Raghavachari, K.; Rendell, A.; Burant, J. C.; Iyengar, S. S.; Tomasi, J.; Cossi, M.; Rega, N.; Millam, J. M.; Klene, M.; Knox, J. E.; Cross, J. B.; Bakken, V.; Adamo, C.; Jaramillo, J.; Gomperts, R.; Stratmann, R. E.; Yazyev, O.; Austin, A. J.; Cammi, R.; Pomelli, C.; Ochterski, J. W.; Martin, R. L.; Morokuma, K.; Zakrzewski, V. G.; Voth, G. A.; Salvador, P.; Dannenberg, J. J.; Dapprich, S.; Daniels, A. D.; Farkas; Foresman, J. B.; Ortiz, J. V.; Cioslowski, J.; Fox, D. J. *Gaussian09*; Gaussian, Inc.: Wallingford, CT, 2009.
(32) Northrop, D. B. *Biochemistry* **1975**, *14*, 2644.
(33) Northrop, D. B. *Annu. Rev. Biochem.* **1981**, *50*, 103.
(34) Zhang, Y.; Luo, M.; Schramm, V. L. *J. Am. Chem. Soc.* **2009**, *131*, 4685.
(35) Berti, P. J.; Tanaka, K. S. E. *Adv. Phys. Org. Chem.* **2002**, *37*, 239.
(36) Glad, S. S.; Jensen, F. *J. Am. Chem. Soc.* **1997**, *119*, 227.
(37) Sunko, D. E.; Szele, I.; Hehre, W. J. *J. Am. Chem. Soc.* **1977**, *99*, 5000.
(38) Becke, A. D. *J. Chem. Phys.* **1993**, *98*, 5648.
(39) Himo, F.; Siegbahn, P. E. *J. Am. Chem. Soc.* **2001**, *123*, 10280.
(40) Kahraman, A.; Morris, R. J.; Laskowski, R. A.; Favia, A. D.; Thornton, J. M. *Proteins* **2010**, *78*, 1120.
(41) Singh, V.; Evans, G. B.; Lenz, D. H.; Mason, J. M.; Clinch, K.; Mee, S.; Painter, G. F.; Tyler, P. C.; Furneaux, R. H.; Lee, J. E.; Howell, P. L.; Schramm, V. L. *J. Biol. Chem.* **2005**, *280*, 18265.
(42) Saen-Oon, S.; Quaytman-Machleder, S.; Schramm, V. L.; Schwartz, S. D. *Proc. Natl. Acad. Sci. U.S.A.* **2008**, *105*, 16543.
(43) Parikh, S. L.; Schramm, V. L. *Biochemistry* **2004**, *43*, 1204.
(44) Bell, C. E.; Eisenberg, D. *Biochemistry* **1996**, *35*, 1137.
(45) Kahn, K.; Bruice, T. C. *J. Am. Chem. Soc.* **2001**, *123*, 11960.

(46) Handlon, A. L.; Xu, C.; Muller-Steffner, H. M.; Schuber, F.; Oppenheimer, N. J. *J. Am. Chem. Soc.* **1994**, *116*, 12087.
(47) Mazzella, L. J.; Parkin, D. W.; Tyler, P. C.; Furneaux, R. H.; Schramm, V. L. *J. Am. Chem. Soc.* **1996**, *118*, 2111.
(48) Zhang, Y.; Deng, H.; Schramm, V. L. *J. Am. Chem. Soc.* **2010**, *132*, 17023.
(49) Berti, P. J.; Blanke, S. R.; Schramm, V. L. *J. Am. Chem. Soc.* **1997**, *119*, 12079.
(50) Scheuring, J.; Schramm, V. L. *Biochemistry* **1997**, *36*, 4526.
(51) Scheuring, J.; Berti, P. J.; Schramm, V. L. *Biochemistry* **1998**, *37*, 2748.
(52) Scheuring, J.; Schramm, V. L. *Biochemistry* **1997**, *36*, 8215.